frontiers | Frontiers in Astronomy and Space Sciences

ORIGINAL RESEARCH
published: 23 June 2022
doi: 10.3389/fspas.2022.908730

Electron Anisotropies in Magnetotail Dipolarization Events

Joachim Birn[1,2]*, *Michael Hesse*[3] and *Andrei Runov*[4]

[1]Space Science Institute, Boulder, CO, United States, [2]Guest Scientist, Los Alamos National Laboratory, Los Alamos, NM, United States, [3]NASA Ames Research Center, Moffett Field, CA, United States, [4]Department of Earth, Planetary, and Space Sciences, University of California, Los Angeles, Los Angeles, CA, United States

Anisotropic electron distributions can be a major source of free energy for the generation of microinstabilities and waves. Here we investigate specifically anisotropies of the suprathermal electrons associated with dipolarization events in the geomagnetic tail. The investigation is based on an MHD simulation of magnetotail reconnection, flow bursts and dipolarization. This simulation is used to trace test particles in the electromagnetic fields of the MHD simulation and investigate their acceleration and contributions to flux increases. The simulated velocity distributions yield anisotropies which can be dominantly parallel ("cigar"-shaped), perpendicular ("pancake"-shaped) to the magnetic field, or a combination thereof (e.g., "rolling-pin"-shaped), depending on location, relative timing, and energy.

Keywords: electron anisotropies, particle acceleration, dipolarization events, magnetospheric substorms, particle sources

OPEN ACCESS

Edited by:
Charles William Smith, University of New Hampshire, United States

Reviewed by:
Thomas Earle Moore, Third Rock Research, United States
Agnit Mukhopadhyay, National Aeronautics and Space Administration, United States

***Correspondence:**
Joachim Birn
jbirn@spacescience.org

Specialty section:
This article was submitted to Space Physics, a section of the journal Frontiers in Astronomy and Space Sciences

Received: *30 March 2022*
Accepted: *30 May 2022*
Published: *23 June 2022*

Citation:
Birn J, Hesse M and Runov A (2022) Electron Anisotropies in Magnetotail Dipolarization Events. Front. Astron. Space Sci. 9:908730. doi: 10.3389/fspas.2022.908730

1 INTRODUCTION

Charged particle flux increases at suprathermal energies of tens to hundreds of keV are a typical signature of dipolarization events in the near magnetotail, associated with substorms and other activity (e.g., Lezniak et al., 1968; Parks and Winckler, 1968; Arnoldy and Chan, 1969; Baker et al., 1978; Belian et al., 1981; Nakamura et al., 2002; Runov et al., 2009; Sergeev et al., 2009; Deng et al., 2010; Fu et al., 2020). In the tail region beyond about 10 R_E distance, these events are commonly associated with earthward flow bursts, which are most likely caused by reconnection events farther tailward. They are characterized by a rapid increase of the normal magnetic field B_z (dipolarization front, "DF"), indicating a transient or permanent change from a stretched, tail-like, to a more dipolar magnetic field configuration. The region of enhanced B_z immediately after the DF has been named "dipolarizing flux bundle" (DFB) (Liu et al., 2013) or "flux pileup region" (FPR) (e.g., Khotyaintsev et al., 2011). A plausible interpretation identifies DFBs with entropy-depleted magnetic flux tubes (Sergeev et al., 1996; Wolf et al., 2009), originally proposed by Pontius and Wolf (1990) and also called "bubbles." They are likely caused by the severance, via reconnection, of parts of closed field lines, which are ejected tailward as "plasmoids" (e.g., Hones, 1979). The likely mechanism of the energetic particle flux increases is the acceleration of charged particles by the localized cross-tail electric field associated with a flow burst and dipolarization. This conclusion is supported particularly by particle tracing in analytic or numerically simulated electric field pulses associated with localized flow bursts (Zelenyi et al., 1990; Birn et al., 1997, 1998, 2004; Li et al., 1998; Zaharia et al., 2000; Ashour-Abdalla et al., 2011; Gabrielse et al., 2012; Pan et al., 2014; Artemyev et al., 2015; Gabrielse et al., 2016).

The major acceleration mechanisms affecting electrons are direct acceleration by the electric field in regions of low magnetic field strength, as well as betatron and Fermi acceleration, which affect

electrons more adiabatically. In the reconnection/dipolarization scenario, the direct acceleration is likely confined to the vicinity of the reconnection site, such that betatron and Fermi acceleration in the collapsing DFB are the most likely candidates (e.g., Fu et al., 2020, and references therein). Each mechanism may dominate at different times or in different regions, causing anisotropies of the distribution functions, which could provide free energy for microscopic waves and instabilities. The observed velocity distributions exhibit anisotropies that can be dominantly parallel ("cigar"-shaped), perpendicular ("pancake"-shaped) to the magnetic field, or a combination thereof (e.g., "rolling-pin"-shaped) (e.g., Liu et al., 2017, 2020).

Fu et al. (2011), using Cluster data in the region ~15 R_E downtail, found an association between pancake shaped distributions with "growing" FPRs, defined by increasing earthward flow velocity at the front and cigar-shaped distributions with "decaying" FPRs, defined by a peak of velocity coincident with the DF. On the basis of "Time History of Events and Macroscale Interactions during Substorms" (THEMIS) observations at distances of 11–14 R_E, Runov et al. (2013) found that suprathermal (< 30 keV) electron distributions at DFs were of pancake type near the neutral sheet ($|B_x| < 5$ nT) and mainly cigar type away from the neutral sheet at $|B_x| > 10$ nT. In theses cases, the plasma flow speed peaked just before or at the DF, thus satisfying the definition of a decaying FPR. Wu et al. (2013), using THEMIS electron data > 30keV between 10 and 25 R_E distance downtail, found a dominance of perpendicular anisotropy (indicating betatron acceleration) beyond 15 R_E, but dominance of parallel anisotropy (indicating Fermi acceleration), closer to Earth. Energetic electron distributions with triple peaks at 0, 90, and 180° pitch angles have been identified right after DFs by various observations and simulations (Runov et al., 2012; Wu et al., 2013; Birn et al., 2014; Liu et al., 2017). Liu et al. (2017) attributed the formation of such ("rolling pin") distributions to a mixture of Fermi acceleration in a field line collapsing earthward from the reconnection site, considered "global," and local betatron acceleration in the rapid field increase closer to Earth. They argued that this process should work only above 26 keV.

Such anisotropies may be the source of free energy driving microinstabilities and waves (Gary, 1993; Gary et al., 2014; Gary, 2015). Such waves, on one hand, would tend to reduce or limit the anisotropies (Khotyaintsev et al., 2011; Zhang et al., 2018) but, on the other, can also be a source of energy transport in the form of Poynting flux away from a DFB/FPR (Le Contel et al., 2009). Specifically, perpendicular electron anisotropies in the DFB region behind the front may be the source of whistler waves (Le Contel et al., 2009; Deng et al., 2010; Khotyaintsev et al., 2011; Viberg et al., 2014; Li et al., 2015; Breuillard et al., 2016; Le Contel et al., 2017) or electron-cyclotron waves (Zhou et al., 2009).

Using the three-dimensional time-dependent electric and magnetic field from MHD simulations of near-tail reconnection and flow bursts as basis for test particle studies, we have previously investigated electron acceleration associated with dipolarizations, identified acceleration mechanisms and source regions, and provided insights into spatial and temporal variations of electron and ion fluxes (Birn et al., 1997, 2004, 2013). These simulations also indicated energetic electron anisotropies with a dominance of perpendicular fluxes farther down the tail and closer to the equatorial plane, but an increasing importance of parallel anisotropy closer to Earth and at higher latitudes. In addition, a triple peak structure of flux increases near 0°, 90°, and 180° was found, which has been denoted a "rolling pin" distribution (Liu et al., 2017).

In the present paper we further investigate electron acceleration and flux properties, extending the results of Birn et al. (2013), and Birn et al. (2014) on the basis of the same MHD simulation (Birn et al., 2011). In **Section 2** we summarize major features of the MHD simulation and the test particle simulation approach. We focus on features in three different regions, the plasma sheet boundary layer, the inner flux pileup region earthward of an approaching and stopping bubble, and the stopping region of a DFB farther tailward that is reached by reconnected fields. **Section 3** demonstrates pitch angle variations and **Section 4** characteristic velocity distributions obtained from the test particle approach. **Section 5** then illustrates typical orbits and acceleration mechanisms affecting the distributions with a summary and discussion givrn in **Section 6**.

2 SIMULATION APPROACH

Our approach is based on a combination of a three-dimensional MHD simulation of near-tail reconnection and field collapse (Birn et al., 2011) with particle tracing in the fields of this simulation. Dimensionless units were used throughout. As in earlier papers, a realistic conversion to dimensional units may be based on a magnetic field unit (lobe field at the location of x-line formation) B_n = 12.6 nT, velocity (Alfvén speed) v_n = 1,000 km/s, and length unit of $L_n = 1.5R_E$, leading to a time unit ("Alfvén time") $t_n = L_n/v_n \approx 10$ s, and electric field $E_n = v_nB_n$ = 12.6 mV/m and an energy unit $W_n = \frac{1}{2}m_pv_n^2$ = 5.2keV, where m_p is the proton mass. The simulation covers the region $0 \geq x \geq -60$, $|y| \leq 40$, $|z| \leq 10$ with a 3D dipole located outside the box at $x = 5$, $y = z = 0$. The plasma pressure is normalized by $p_n = B_n^2/\mu_0$. Based on the chosen units, the inner boundary corresponds to $x_{GSM} = -7.5R_E$ and the outer boundary to $x_{GSM} = -97.5R_E$. However, for specific applications, other units may be more appropriate; therefore in the following we will mostly use dimensionless units.

The dynamic evolution was preceded by a period of external driving, which lasted until $t = 61$, leading to the formation of a thin embedded sheet of intensified current density in the near tail peaked around $x = -10$. In the following we will refer to the configuration at $t = 61$ as the "initial state." At this time a finite resistivity was imposed, localized in the region of enhanced current density, which was kept constant in time. (Birn et al., 2011). **Figure 1A** shows magnetic flux contours in the x, z plane at this time together with the initial pressure, which is used to categorize characteristic source regions, as indicated in **Figure 1B**: the inner central plasma sheet (CPS, red color), the outer CPS (orange), the plasma sheet boundary layers; ayer (PSBL, green) and the lobes (light blue). The dynamic evolution after $t = 61$ led to the formation of a neutral line ($B_z = 0$ line) at $t \approx 90$ and the initiation of slow reconnection. Faster reconnection and the generation of fast flows started at $t \approx 125$,

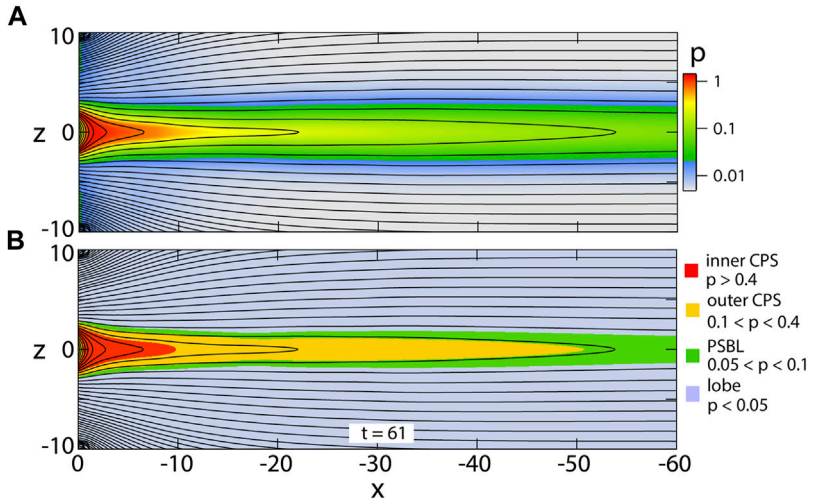

FIGURE 1 | Initial state after completion of the driving period, **(A)** magnetic flux contours and pressure (color) in the *x*, *z* plane at $t = 61$; **(B)** characteristic source regions defined by the initial pressure as indicated in the right margin: inner central plasma sheet (CPS), outer central plasma sheet, plasma sheet boundary layer (PSBL), and lobe.

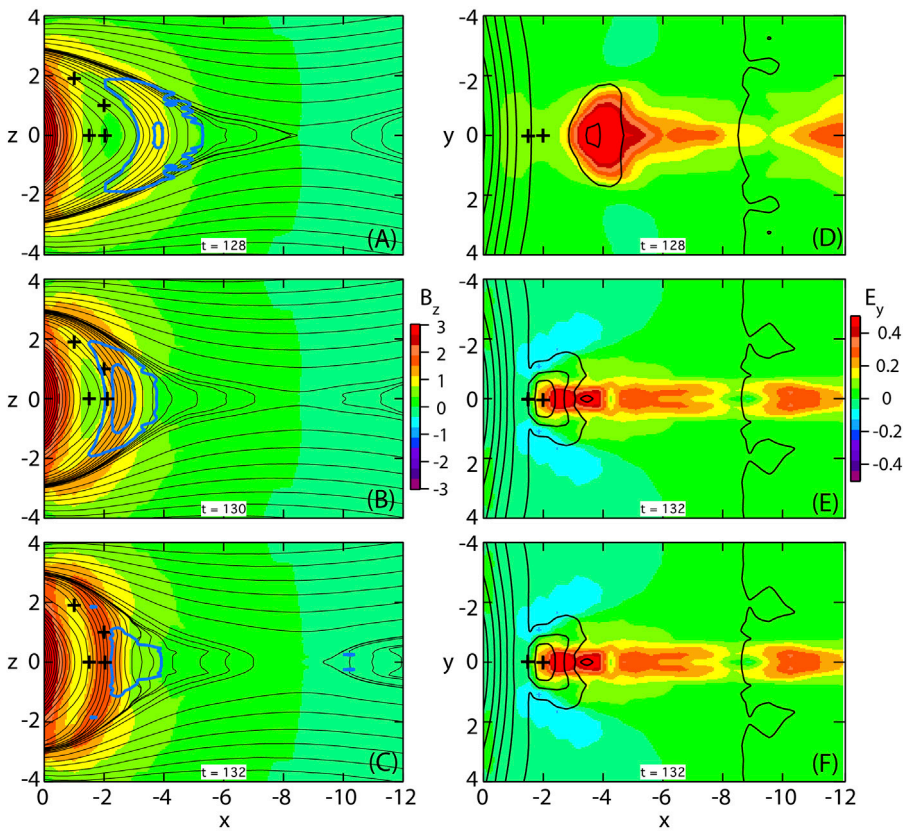

FIGURE 2 | Propagation of a DFB obtained form the MHD simulation. The left column **(A–C)** shows in color the magnetic field component B_z in the *x*, *z* plane together with magnetic flux contours (black lines). The heavy blue contours show the enhanced cross-tail electric field at intervals of 0.4 and the plus signs indicate locations where energetic electron fluxes are evaluated. The right column **(D–F)** shows in color the electric field component E_y in the *x*, *y* plane together with contours of B_z at intervals of 0.5.

when reconnection proceeded to the lobes, presumably due to a combination of reconnection with ballooning/interchange type modes, which were enabled by the reduced entropy of reconnected lobe magnetic flux tubes, which were shortened from plasmoid ejection (Birn et al., 2011, 2015).

Figure 2 illustrates the fast evolution, showing the propagation of a DFB. The color in the left column shows the magnetic field component B_z in the x, z plane together with magnetic flux contours (black lines). The heavy blue contours indicate the enhanced cross-tail electric field, and the plus signs indicate locations where energetic electron fluxes are evaluated. The color in the right column shows the electric field component E_y in the x, y plane together with contours of constant B_z; the contour near $x = -9$ is the $B_z = 0$ line, referred to as x-line. The DFB is indicated by the yellow and red color in **Figures 2A–C** and by a propagating contour in **Figures 2D–F**. It is limited in x and y to a few R_E, consistent with observations (e.g., Nakamura et al., 2004). It comes to rest and actually bounces back after about t = 132, also consistent with observations (Panov et al., 2010a; Panov et al., 2010b; Nakamura et al., 2012; Panov et al., 2013). It is characterized by a cross-tail electric field that far exceeds the reconnection electric field, which is of the order of 0.1, consistent with "fast reconnection" (e.g., Birn et al., 2001). (Our normalization is based on units near the location of the x-line.) The locations indicated by plus signs become enveloped by the DFB after $t \approx 132$. They are chosen to represent three characteristic regions: the location (−1,0,1.9) represents a PSBL location; the others correspond to central plasma sheet locations close to the stopping region, (−1.5,0) is just inward of the region reached by reconnected field lines, while (−2,0,0) and (−2,0,1) are reached even by reconnected lobe field lines, as concluded from the MHD simulation. The latter two locations are right at the equatorial plane and somewhat off the equator.

The orbit integration procedure was discussed in detail by Birn et al. (2004) and Birn et al. (2014). Here we repeat some major facts. The MHD results were saved at intervals of 1 Alfvén time (800 time steps, corresponding to ~ 10s for the chosen units). The orbits were integrated numerically, using linear interpolation between the stored time steps of the MHD fields. Electron orbits were integrated relativistically, using a combination of full orbits and gyro-drift orbits, based on conservation of the magnetic moment μ. The switch between the procedures was based on the magnitude of an adiabaticity parameter [ratio between field line curvature radius and gyoradius (Büchner and Zelenyi, 1989; Birn et al., 2004)]. We note that drift orbit continuity requires a cubic spline interpolation of the magnetic field in space, which could lead to artificial local maxima and minima. To avoid this, a monotonicity-conserving algorithm was employed (Hyman, 1983).

A backward tracing technique (Curran and Goertz, 1989) was used to integrate orbits from selected "final" times and locations backward in time until they reached the initial state (t = 61) or a boundary of the simulation box, using mirroring at the inner boundary x = 0. We then applied Liouville's theorem of the conservation of phase space density F along a phase space trajectory to calculate F values and differential energy fluxes at the final destination from the initial and boundary values at the "source" locations. A full distribution function at the chosen final location and time can then be obtained by varying the final energy and pitch angle. Time profiles of fluxes at selected locations, energies and pitch angles are obtained by varying the times from which particles are launched backwards.

The Validity of the backward tracing is based on the absence of collisions and becomes questionable when collisional regions are encountered. In our case one might consider the regions of low magnetic field, where orbits can undergo pitch angle scattering and our integrations change between drift orbits and full orbits as such regions. We found out, however, that this was not significant. Whereas pitch angles were conserved at these transitions, by accident we had initially set new phase angles to zero for continuing full orbits. Replacing that with random phase angles as intended did change some individual orbits significantly, but did not alter the characteristic pattern of the distributions.

Since the MHD simulation does not provide electron information (other than density, which should equal ion density), particular choices must be made in defining the initial and boundary electron distributions at the source locations. For the results reported here, we again imposed isotropic kappa-distributions (Vasyliunas, 1968; Christon et al., 1988; Christon et al., 1989)

$$F(W_0) \propto n_0 \left(1 + \frac{W_0}{(\kappa - 3/2)kT_e}\right)^{-\kappa-1} \tag{1}$$

with a κ value of 4.5 and chose a fixed initial and boundary temperature kT_e = 0.5 keV. Liouville's theorem of the conservation of F along a phase space trajectory implies that the final distribution is related to the source by

$$F(W) \propto n_0 \left(1 + \frac{W - \Delta W}{(\kappa - 3/2)kT_e}\right)^{-\kappa-1} \tag{2}$$

where ΔW is the energy gain (or loss) along the trajectory. Flux enhancements therefore are directly related to the energy gain and the density n_0 of the source plasma.

We note that the electron velocities were normalized by

$$v_{ne} = \left(m_p/m_e\right)^{1/2} v_n = 42,850\,\mathrm{km/s} \tag{3}$$

where m_p and m_e denote proton and electron mass, respectively. The (normalized) kinetic energy of an electron is then given, in the relativistic approach, by

$$W_k = \frac{1}{\epsilon}(\gamma - 1) \quad \text{with} \qquad \epsilon = W_n \Big/ \left(m_e c^2\right) \tag{4}$$

where

$$\gamma = \sqrt{1 + 2\epsilon u^2} \tag{5}$$

and u is the normalized electron velocity, given by

$$\begin{aligned} u^2 &= u_x^2 + u_y^2 + u_z^2 \qquad \text{(full orbit)} \\ u^2 &= u_\parallel^2 + u_\perp^2 \quad \text{with} \quad u_\perp^2 = \mu B \qquad \text{(drift orbit)} \end{aligned} \tag{6}$$

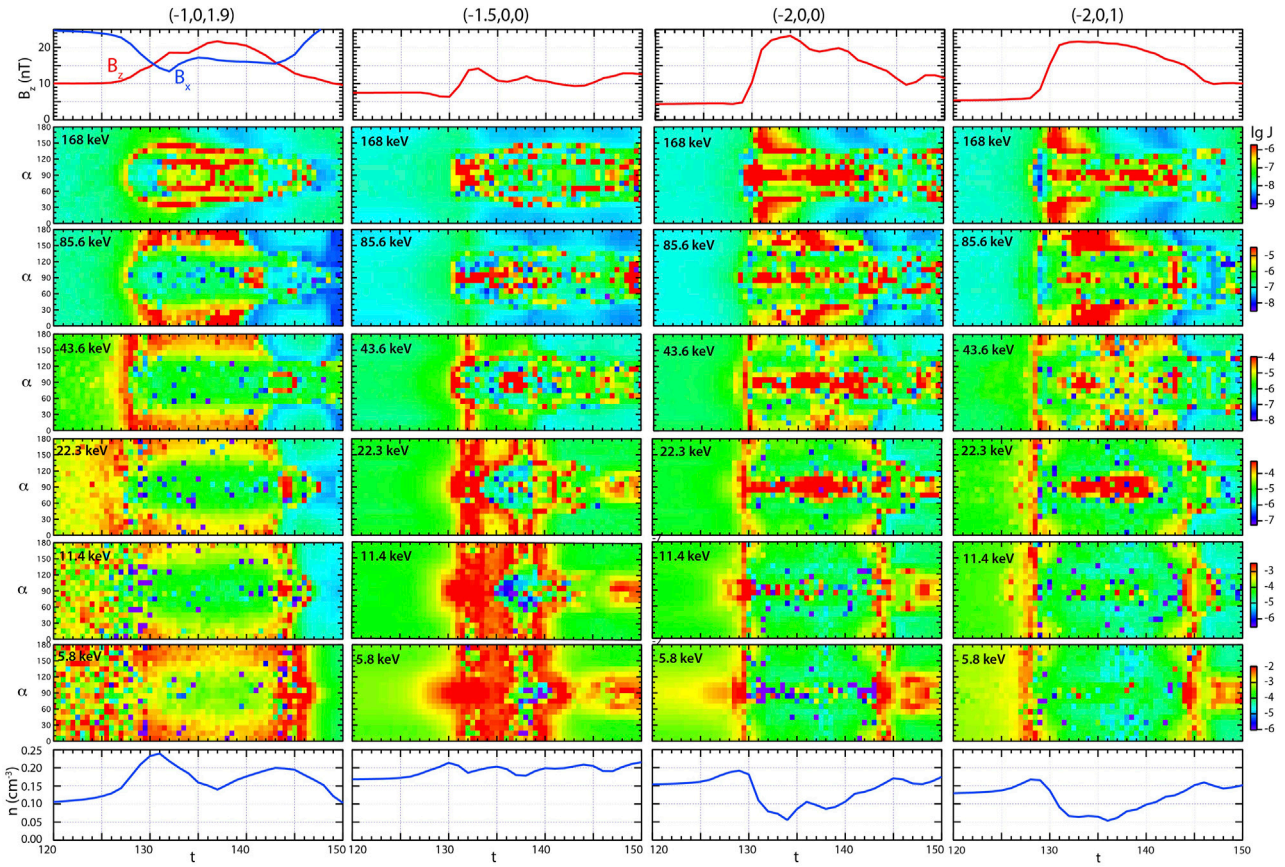

FIGURE 3 | Simulated electron fluxes as functions of time and pitch angle at four selected locations indicated on top. Different energies are indicated in the colored panels. The top and bottom panels show the magnetic field B_z (in red) and the plasma density n, respectively, at the three locations. For the PSBL location, (-1, 0, 1.9), the magnetic field component B_x is also added (blue curve, top left panel).

where μ is the normalized relativistic magnetic moment (Birn et al., 2004).

Our orbit integration includes several modifications from the approach described in Birn et al. (2004) and Birn et al. (2014):

1) The particle reflection at the inner boundary of the simulation box now takes into account a finite time of travel to the actual mirror point outside the box closer to Earth. This delay time was estimated by using a Tsyganenko model (Tsyganenko, 1987) to calculate this travel time based on the velocity and pitch angle at the inner boundary. This affected primarily particles at low pitch angles. As a consequence, they exhibit fewer bounces than if they are immediately reflected back into the box, reducing the number of neutral sheet crossing, which are the dominant source of Fermi acceleration type B (Northrop, 1963).
2) The linear interpolation of the electromagnetic fields between the finite grid points could lead to spurious parallel electric fields. This effect was eliminated by separating the electric field into a field-aligned and a perpendicular component, and interpolating the two individually. We found, however, that this affected only very few orbits and did not alter the distributions in a noticeable way.
3) We discovered that the fluxes and phase space densities shown in Birn et al. (2014) were inadvertently evaluated with $\kappa = 2.5$ rather than $\kappa = 4.5$ as stated in the paper. This has no effect on the particle orbits, however, nor on the qualitative features shown. The only effect is to raise the numerical values at high energies.

3 PITCH ANGLE DISTRIBUTIONS

The variations of electron fluxes at the four selected locations (indicated on top of the panels) are shown in **Figure 3** as functions of time and pitch angle for several energies, together with the variations of B_z (top, red curves) and plasma density (bottom) obtained from the MHD simulation. The energies are labeled based on our normalization factor W_n = 5.22 keV. (A different choice of v_n could reduce those energies, for instance v_n = 500 km/s, W_n = 1.30 keV, would reduce the energies by a factor 1/4.)

The MHD results (top and bottom) in **Figure 3** show characteristically different signatures at the selected locations. The B_z increase at the PSBL location (red curve, top left panel) is more gradual than at the equator; it goes together with an entry deeper into the plasma sheet, as shown by the decrease of B_x (blue

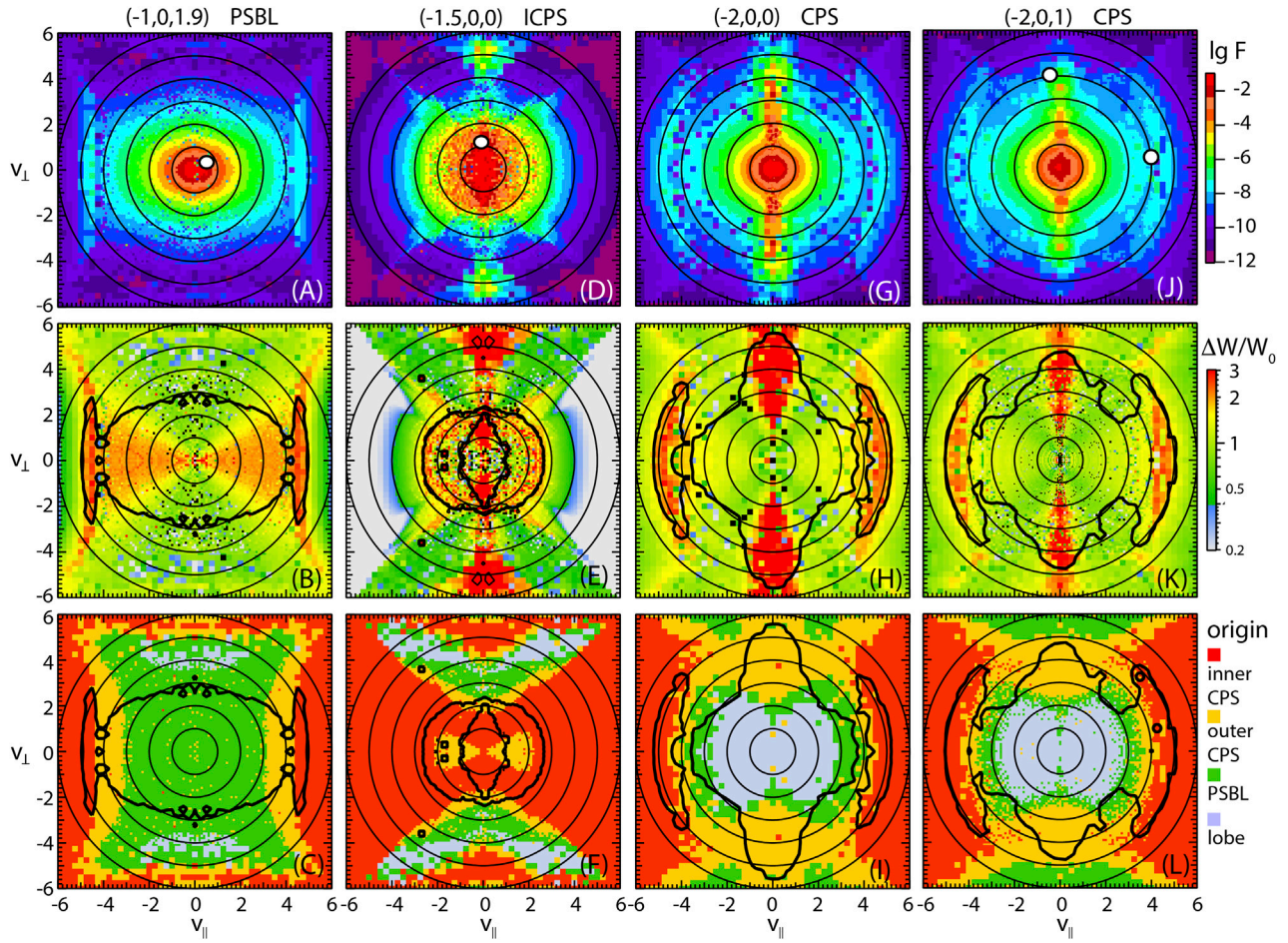

FIGURE 4 | Electron velocity distributions at chosen location for $t = 132$: **(top row, a, d, g, j)** phase space density, **(second row, b, e, h, k)** relative energy gain, and **(third row, c, f, i, l)** origin of particles contributing to the phase space density. For the chosen normalization, the velocity unit is given by **(3)** as 42,850 km/s. The heavy black contours indicate the regions of enhanced F (top row) and the white dots in the top panels show final velocities used to illustrate characteristic orbits in **Section 5**.

curve in the top left panel) and the density increase (bottom left panel). These features have been reported earlier in the context of energetic ion fluxes (Birn et al., 2017).

The inner CPS location (second column), which is not reached by reconnected, depleted flux tubes at the time of dipolarization, shows a more modest increase of B_z than the two locations farther tailward (third and fourth column). It also shows a slight increase in density (bottom panel), resulting from a compression of preexisting plasma sheet plasma, whereas the two locations farther out show a decrease, which is more typical (Runov et al., 2011) and consistent with the arrival of depleted reconnected PSBL and lobe flux tubes.

At low energies of a few keV the energetic electron fluxes reflect the behavior of the MHD plasma density at all locations, showing a drop when the plasma density is reduced and an increase at the innermost CPS location. At higher energies, the results are different. The PSBL location (left column) is characterized by a very brief increase, which tends to start near 90° but then rapidly spreads to all pitch angles. This is followed by a persistent increase around 0 and 180° at most energies. Only at the highest one of 168 keV the distribution becomes more complicated, with double peaks around 45 and 135°.

The inner CPS location (second column) up to ~23 keV is characterized by an enhancement of fluxes, which also starts around 90°. It is interrupted by a brief decrease around $t = 137$. A closer inspection (not shown here) indicates that this is due to the arrival of reconnected field lines, which carry plasma from the more distant tail and, at higher energies, PSBL and lobes. The highest energies show a more persistent enhancement around 90°.

The outer two CPS locations (third and fourth column) show very similar features. The third column corresponds to the results shown in the left column of Figure 4 in Birn et al. (2014) with the modifications discussed in **Section 2**. The qualitative features are not changed by those modifications. The major difference is a change of scales, which results from the steeper slope of the source energy distribution associated with the larger kappa value. Fluxes at 22.3 keV show a persistent perpendicular anisotropy (peak near 90°), after a very brief nearly isotropic enhancement. In contrast the higher energies show the triple peak (rolling pin)

structure at 0, 90, and 180°, discussed already by Birn et al. (2014). Interestingly, at the highest energy, the peaks at 0 and 180° tend to move away from the field-aligned direction toward 45 and 135° after the dipolarization.

4 VELOCITY DISTRIBUTIONS

Figure 4 shows velocity distributions at the chosen locations for t = 132, right after the dipolarization, which is the period most commonly investigated in observations. We note that each pixel again corresponds to a single trajectory mapping the source phase space density to the final location. This allows us to identify the relative energy gain $\Delta W/W_0$ (second row) as the main contribution to flux enhancements, where W_0 is the energy at the initial location, and the particle origins (bottom row), as defined in **Figure 1**. We note that both of these quantities do not depend on the assumed source distributions; they are simply a consequence of the orbits governed by the MHD electric and magnetic fields.

The distributions in **Figure 4** show characteristic differences, as well as some commonalities. The PSBL distribution (**Figure 4A**) shows the field-aligned anisotropy already demonstrated by **Figure 3** (left column). This extends also to two counter streaming beams, which, however, may not be distinct in observed distributions. They are slightly more enhanced relative to the lower energies because of their origin in the inner CPS, where the densities are higher (**Figure 4C**). Such beams are also present in the CPS distributions at x = −2 (**Figures 4G,J**) with similar origin in the inner CPS (**Figures 4I,L**). The distribution just earthward of the stopping (**Figure 4D**) does not show such beams. However, all CPS distributions show strong ring-like perpendicular anisotropies. For the outer locations, x = −2, the particles originate primarily from the outer CPS (orange color in **Figures 4I,L**, while hte contributions at the inner location x = −1.5 come predominantly from the inner CPS (red color in **Figure 4F**).

Overall, the contributions to the distribution at the inner location x = −1.5 come from the inner CPS, consistent with the conclusion from the MHD simulation that reconnected field lines do not reach this location. There is an inner region of the distribution just inside the almost circular contour in **Figure 4E** at $v \approx 2$ (corresponding to about 20 keV) that appears almost uniformly energized by factors $\Delta W/W_0 \approx 2$ enclosing the strongly anisotropic disk at lower energy. This appears to be region that is adiabatically compressed earthward of the DFB itself and roughly isotropically heated.

In the CPS distributions farther out there are similar regions of lobe origin (light blue color in (**Figures 4I,L**) that are also energized, but by smaller gains ($\Delta W/W_0 \approx 1$ corresponding to doubling the energy), representing the nearly isotropic cores of the distributions. Their origin is again consistent with a result from lobe field reconnection, inferred from the MHD simulation.

5 CHARACTERISTIC ORBITS

Figure 4 already provided some basic facts about the history and origin of the accelerated particles contributing to the enhanced energetic electron fluxes. However, it is instructive to illustrate these with specific orbits.

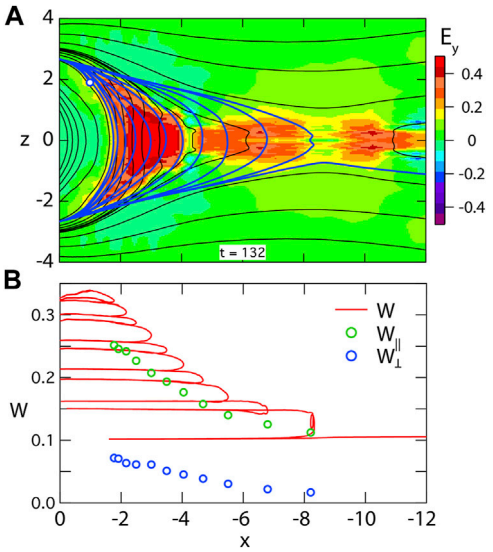

FIGURE 5 | Electron orbit contributing to the enhanced field-aligned fluxes at the PSBL location (−1, 0, 1.9), **(A)** projection of the orbit into the x, z plane superposed on the color-coded electric field at t = 132, **(B)** particle energy as function of x (red curve) together with the parallel (green circles) and perpendicular (blue circles) components at the equatorial crossings.

5.1 Field-Aligned Electrons in the PSBL

Details of the acceleration mechanism have been discussed previously by Birn et al. (2004, 2012). It is essentially the same at all energies. We therefore illustrate it in **Figure 5** for a particle at relatively low energy, close to the initial thermal energy of 0.1 (corresponding to ~0.52 keV for our chosen units). The particle originates from a closed field line extending into the more distant tail. It becomes trapped in the inner tail when the field line becomes reconnected and bounces several times while participating in the field collapse. **Figure 5B** demonstrates that the acceleration takes place at neutral sheet crossings, to be interpreted as first-order Fermi acceleration of type B (Northrop, 1963), akin to a slingshot effect in the curved earthward moving magnetic field. The parallel acceleration can equally well be interpreted as **E**×**B** drift in the direction of the magnetic field curvature vector or as curvature drift in the direction opposite to the cross-tail electric field E_y (Birn et al., 2013).

The particle illustrated in **Figure 5** also has a small perpendicular drift velocity component, which becomes enhanced at each neutral sheet crossing as well (Blue circles). This acceleration can be attributed to the betatron effect, which can also be interpreted in two ways (Birn et al., 2013): as **E** ×**B** drift in the direction of increasing magnetic field strength or as gradient B drift in the direction opposite to the cross-tail electric field.

5.2 Perpendicular Electrons in the Inner Pileup Region

Figure 6 illustrates the history of a particle contributing to the perpendicular anisotropy in the inner pileup region. This is a

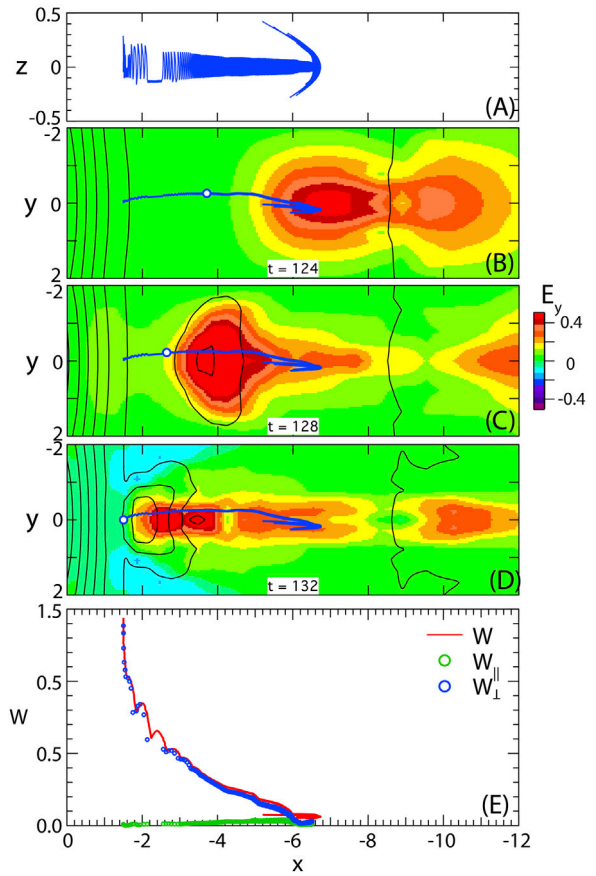

FIGURE 6 | Electron drift orbit contributing to the enhanced perpendicular fluxes at the inner location (−1.5, 0, 0), **(A)** projection of the orbit into the *x*, *z* plane, **(B–D)** orbit in the *x*, *y* plane, superposed on snapshots of the color-coded electric field and particle location (white dot) at *t* = 124, 128, 132, **(E)** particle energy as function of *x* (red curve) together with the parallel (green circles) and perpendicular (blue circles) components.

particle of initially thermal energy, less than 0.1, being almost at rest in the inner tail. It gets "scooped up" in front of the approaching DFB (**Figures 6B–D**) and experiences betatron acceleration from the magnetic field increase that also affects the field in front of the DFB flow bursts. As illustrated by **Figure 6A**, the particle initially exhibits a wider bounce near $x = -6$, before it its pitch angle gets scattered and it continues on a narrow bounce around $z = 0$ toward its final location at $x = -1.5$. For a brief period, near $x = -2.5$, it stays below the equatorial plane $z = 0$. This is due to the fact that the magnetic field at this time and location becomes indented (**Figure 2C**) such that the particle becomes trapped in a field minimum below $z = 0$.

5.3 DFB Orbits

Figure 7 contrasts the history of particles contributing to the high-energy field-aligned beams and the perpendicular fluxes in the CPS region of the DFB. These particles contribute to the peaks of the fluxes at 0, 90, and 180° described as rolling pin distributions (Liu et al., 2017). It is instructive to follow the two orbits backward in time from their final location at $t = 132$, focusing on the drift in the equatorial plane (**Figures 7B–D**). Note that the red/pink curves are close to the actual equatorial drift of the ~ 90° pitch angle particle, while the blue curves in **Figures 7B–D** represent only the equatorial crossing points of the multi-bounce orbit shown in **Figure 7A**. In either case the displacement in the *y* direction is related to their respective gradient or curvature drift, while the motion in the *x* direction is determined by the **E** ×**B** drift, which is similar in both cases but varies slightly according to the finite extent and variation in *y* of B_z and E_y, visible in **Figures 7B–D**.

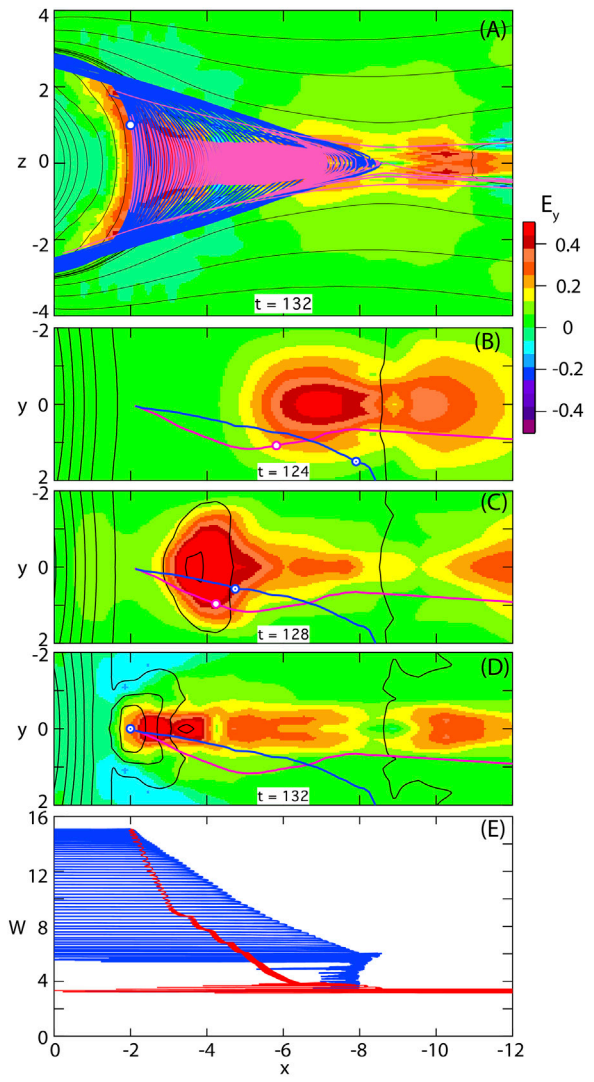

FIGURE 7 | Electron orbits contributing to the enhanced CPS fluxes at (−2, 0, 1). Blue curves represent an electron contributing to the field-aligned beam, red/pink curves correspond to a ~ 90° pitch angle orbit contributing to the enhanced perpendicular fluxes; **(A)** projection of the orbits into the *x*, *z* plane, **(B–D)** equatorial crossing points of the orbits in the *x*, *y* plane, superposed on snapshots of the color-coded electric field, with the particle locations at *t* = 124, 128, 132 shown as white dots; **(E)** particle energies as function of *x*.

The magnetic field gradient near the final, more dipolar, location is steep, while the curvature is weak. Therefore the gradient drift is stronger than the curvature drift and ~ 90° pitch angle particle (red curve) gets more displaced in the y direction than the ~ 0° pitch angle particle (blue curve). It also looses more energy (actually, gains in forward tracing) such that its energy is significantly lower at the entry into the acceleration region around t = 124 (**Figure 7B**). At this point the ~ 0° pitch angle particle still has a high energy of ~6, the magnetic field curvature is strong while the magnetic field gradient is weak. As a consequence the curvature drift now becomes dominant for the ~ 0° pitch angle particle, leading back to a source region on the duskside earthward of the neutral line, whereas the ~ 90° pitch angle particle can be traced back toward the neutral line, indicating its source in the closed field region extending farther tailward and its entry into the acceleration region via reconnection.

During the main acceleration, both particles satisfy the adiabaticity criterion. This breaks down in the low-field region in the vicinity of the x-line, such that both particles have undergone a number of pitch angle scatterings prior to the acceleration. Hence there is no correlation between the final pitch angle and the one in the source region. **Figure 7E** indicates that the particle with ~ 0° final pitch angle (blue curve) has changed from a nearly equatorial orbit prior to the entry into the main DFB; it has gained a small amount of energy by betatron acceleration drifting dawnward in the weaker electric field duskward of the region shown in **Figures 7B–D**. In this case both particles have started from similar initial energies, indicating similar final phase space densities. More typically, however, ~ 90° pitch angle particle that originate from the distant plasma sheet haves a lower source energy corresponding to a higher phase space density, when mapped along their trajectory to the final location than the ~ 0° pitch angle particles, which mainly originate on the dusk side. This explains the higher fluxes at ~ 90° pitch angle as compared to the field-aligned beams and thus a net perpendicular anisotropy.

6 SUMMARY AND DISCUSSION

Using a combined MHD/test particle approach, we have further investigated electron acceleration and energetic electron flux increases associated with dipolarization events in the region earthward of a near-tail reconnection site. In modification of earlier approaches we included a delay time from particle mirroring closer to Earth (outside the simulation box) and eliminated potential spurious parallel electric fields from an interpolation procedure. The latter, however, was found insignificant.

Our investigation focused on electron anisotropies, which can be the source of free energy driving microscopic waves and instabilities (e.g., Gary, 1993, 2015; Khotyaintsev et al., 2011), extending earlier results (Birn et al., 2014) particularly by deriving phase space distributions (PSDs) for the time right after dipolarization (that is, the increase of B_z) in three different regions, the plasma sheet boundary layer (PSBL), the inner flux pileup region (inner FPR) in the central plasma sheet (CPS), which is not reached (yet) by reconnected PSBL or lobe field lines, and the outer FPR, which is reached by such field lines. Selected orbits were shown to illustrate the findings in the velocity distributions.

We confirmed that betatron and first-order Fermi acceleration are the dominant acceleration mechanisms, operating in the regime of field collapse, consistent with earlier conclusions (e.g. Smets et al., 1999; Birn et al., 2004; Wu et al., 2006; Fu et al., 2011, 2020). This happened in the inner region where a drift orbit approximation was found to be valid, based on the conservation of the (relativistic) magnetic moment μ.

The Fermi acceleration, which dominates for small pitch angles, was found to happen at multiple neutral sheet crossings in the curved magnetic field of earthward moving field lines. This has been described as "type B" (Northrop, 1963) akin to a slingshot effect, associated with **E**×**B** drift in the direction of the field curvature vector. This, however, can equally well be described as curvature drift in the direction opposite to the cross-tail electric field (e.g., Birn et al., 2013). As the particle bounces happen on closed magnetic field lines that become shorter as the fields collapse toward Earth, this mechanism is also often described as Fermi acceleration of type A (Northrop, 1963), that is, multiple bounces between approaching mirrors. In that case the acceleration is commonly inferred from the conservation of the second adiabatic invariant. Here, we did not impose (or investigate) this conservation law, and it is an open question to what extent the two interpretations are equivalent quantitatively. The development of field-aligned anisotropy extends not only to high suprathermal energies but also to low sub-keV energies. This fact and the inferred acceleration in the collapsing field are consistent with observations at geosynchronous orbit (e.g., Moore and Arnoldy, 1982), providing a direct source of precipitating auroral electrons.

In addition, betatron acceleration was demonstrated, associated with the **E**×**B** drift in the direction of increasing magnetic field strength. This can also be described by (gradient) drift in the direction opposite to the (main) cross-tail electric field.

Our simulations yielded characteristic differences between the locations. The PSBL location was characterized by strong field-aligned anisotropy extending to high-energy beams. In contrast to the main population, these beams originated from the inner central plasma sheet, entering the acceleration by cross-tail drift, Their pitch angle was typically scattered several times during neutral sheet crossings prior to this entry. Similar beams with the same history were also found at the outer FPR locations in the CPS, however, together with strong enhancements around 90° pitch angles, causing net perpendicular anisotropies, consistent with observations by Runov et al. (2012).

At energies of a few tens of keV, the combination of the field-aligned beams with the perpendicular enhanced fluxes in the CPS resulted in the multi peak structure described as rolling pin distributions (Liu et al., 2017) and found earlier in observations (Runov et al., 2012; Wu et al., 2013) and simulations (Birn et al., 2014). Our results are consistent with conclusions by Liu et al. (2017) that these structures were restricted to energies just above 26 keV. However, Zhao et al. (2019) also observed such

distributions at energies above 1.7 keV. On the basis of our simulations, this difference could be understood by different scenarios with different background parameters. Our results depend on the chosen scaling. Reducing the characteristic velocity v_n by a factor λ would reduce the characteristic energy by λ^2. This could substantially lower the range where the rolling pin distributions are found.

Our simulations also enabled us to identify the source regions of particles contributing to the different final distributions. Particles in the PSBL distributions originated also from the PSBL (on either side). Particles in the inner flux pileup region originated from the inner CPS, were energized primarily through the betatron effect in the compressed plasma. The field-aligned beams were absent in that region.

The origin of the particles contributing to the distributions in the outer FPR/CPS was more complicated. The distributions consisted of an inner core of weakly, more isotropically, energized (i.e, heated) particles of lobe origin, surrounded by a population of outer CPS origin, which was energized by betatron acceleration. These distributions also contained field-aligned beams, which were of inner CPS origin with the same history as the high-energy beams in the PSBL.

Finally, some general comments: The distributions, particularly in the FPR region reached by reconnected lobe field lines, show high variability with time and energy. In evaluating the effects of different acceleration mechanisms it is important not only to consider the earthward transport of particles but also the finite extent and cross-tail variation of the acceleration region.

DATA AVAILABILITY STATEMENT

The datasets presented in this study can be found in online repositories. The names of the repository/repositories and accession number(s) can be found in the article/supplementary material.

AUTHOR CONTRIBUTIONS

JB performed the simulations and prepared the body of the text. MH and AR provided background and contributions to the text.

FUNDING

The simulation work was performed by JB at Los Alamos under the auspices of the US Department of Energy, supported by NASA grant 80NSSC18K0834 and NSF grant 1602655. AR acknowledges support from NASA contract NAS5-02099.

ACKNOWLEDGMENTS

This work is dedicated to the memory of Peter Gary, a close friend and valued advisor, who had a keen interest in the sources of electron anisotropy. The simulation work was performed by JB at Los Alamos under a guest scientist agreement.

REFERENCES

Arnoldy, R. L., and Chan, K. W. (1969). Particle Substorms Observed at the Geostationary Orbit. *J. Geophys. Res.* 74, 5019–5028. doi:10.1029/ja074i021p05019

Artemyev, A. V., Liu, J., Angelopoulos, V., and Runov, A. (2015). Acceleration of Ions by Electric Field Pulses in the Inner Magnetosphere. *J. Geophys. Res. Space Phys.* 120, 4628–4640. doi:10.1002/2015JA021160

Ashour-Abdalla, M., El-Alaoui, M., Goldstein, M. L., Zhou, M., Schriver, D., Richard, R., et al. (2011). Observations and Simulations of Non-local Acceleration of Electrons in Magnetotail Magnetic Reconnection Events. *Nat. Phys.* 7, 360–365. doi:10.1038/nphys1903

Baker, D. N., Higbie, P. R., Hones, E. W., Jr., and Belian, R. D. (1978). High-Resolution Energetic Particle Measurements at 6.6 RE, 3. Low-Energy Electron Anisotropies and Short-Term Substorm Predictions. *J. Geophys. Res.* 83, 4863–4868. doi:10.1029/ja083ia10p04863

Belian, R. D., Baker, D. N., Hones, E. W., Jr., Higbie, P. R., Bame, S. J., and Asbridge, J. R. (1981). Timing of Energetic Proton Enhancements Relative to Magnetospheric Substorm Activity and its Implication for Substorm Theories. *J. Geophys. Res.* 86, 1415. doi:10.1029/ja086ia03p01415

Birn, J., Artemyev, A. V., Baker, D. N., Echim, M., Hoshino, M., and Zelenyi, L. M. (2012). Particle Acceleration in the Magnetotail and Aurora. *Space Sci. Rev.* 173, 49–102. doi:10.1007/s11214-012-9874-4

Birn, J., Chandler, M., Moore, T., and Runov, A. (2017). Ion Velocity Distributions in Dipolarization Events: Beams in the Vicinity of the Plasma Sheet Boundary. *J. Geophys. Res. Space Phys.* 122, 8026–8036. doi:10.1002/2017JA024231

Birn, J., Drake, J. F., Shay, M. A., Rogers, B. N., Denton, R. E., Hesse, M., et al. (2001). Geospace Environmental Modeling (GEM) Magnetic Reconnection Challenge. *J. Geophys. Res.* 106, 3715–3719. doi:10.1029/1999ja900449

Birn, J., Hesse, M., Nakamura, R., and Zaharia, S. (2013). Particle Acceleration in Dipolarization Events. *J. Geophys. Res. Space Phys.* 118, 1960–1971. doi:10.1002/jgra.50132

Birn, J., Liu, Y.-H., Daughton, W., Hesse, M., and Schindler, K. (2015). Reconnection and Interchange Instability in the Near Magnetotail. *Earth Planet Sp.* 67, 110. doi:10.1186/s40623-015-0282-3

Birn, J., Nakamura, R., Panov, E. V., and Hesse, M. (2011). Bursty Bulk Flows and Dipolarization in MHD Simulations of Magnetotail Reconnection. *J. Geophys. Res.* 116, a–n. doi:10.1029/2010JA016083

Birn, J., Runov, A., and Hesse, M. (2014). Energetic Electrons in Dipolarization Events: Spatial Properties and Anisotropy. *J. Geophys. Res. Space Phys.* 119, 3604–3616. doi:10.1002/2013JA019738

Birn, J., Thomsen, M. F., Borovsky, J. E., Reeves, G. D., McComas, D. J., Belian, R. D., et al. (1998). Substorm Electron Injections: Geosynchronous Observations and Test Particle Simulations. *J. Geophys. Res.* 103, 9235–9248. doi:10.1029/97ja02635

Birn, J., Thomsen, M. F., Borovsky, J. E., Reeves, G. D., McComas, D. J., Belian, R. D., et al. (1997). Substorm Ion Injections: Geosynchronous Observations and Test Particle Orbits in Three-Dimensional Dynamic MHD Fields. *J. Geophys. Res.* 102, 2325–2341. doi:10.1029/96ja03032

Birn, J., Thomsen, M. F., and Hesse, M. (2004). Electron Acceleration in the Dynamic Magnetotail: Test Particle Orbits in Three-Dimensional Magnetohydrodynamic Simulation Fields. *Phys. Plasmas* 11, 1825–1833. doi:10.1063/1.1704641

Breuillard, H., Le Contel, O., Retino, A., Chasapis, A., Chust, T., Mirioni, L., et al. (2016). Multispacecraft Analysis of Dipolarization Fronts and Associated Whistler Wave Emissions Using MMS Data. *Geophys. Res. Lett.* 43, 7279–7286. doi:10.1002/2016GL069188

Büchner, J., and Zelenyi, L. M. (1989). Regular and Chaotic Charged Particle Motion in Magnetotaillike Field Reversals: 1. Basic Theory of Trapped Motion. *J. Geophys. Res.* 94, 11821–11842. doi:10.1029/JA094iA09p11821

Christon, S. P., Mitchell, D. G., Williams, D. J., Frank, L. A., Huang, C. Y., and Eastman, T. E. (1988). Energy Spectra of Plasma Sheet Ions and Electrons from ~50 eV/eto ~1 MeV during Plasma Temperature Transitions. *J. Geophys. Res.* 93, 2562. doi:10.1029/ja093ia04p02562

Christon, S. P., Williams, D. J., Mitchell, D. G., Frank, L. A., and Huang, C. Y. (1989). Spectral Characteristics of Plasma Sheet Ion and Electron Populations during Undisturbed Geomagnetic Conditions. *J. Geophys. Res.* 94, 13,409. doi:10.1029/ja094ia10p13409

Curran, D. B., and Goertz, C. K. (1989). Particle Distributions in a Two-Dimensional Reconnection Field Geometry. *J. Geophys. Res.* 94, 272. doi:10.1029/ja094ia01p00272

Deng, X., Ashour-Abdalla, M., Zhou, M., Walker, R., El-Alaoui, M., Angelopoulos, V., et al. (2010). Wave and Particle Characteristics of Earthward Electron Injections Associated with Dipolarization Fronts. *J. Geophys. Res.* 115, a–n. doi:10.1029/2009JA015107

Fu, H., Grigorenko, E. E., Gabrielse, C., Liu, C., Lu, S., Hwang, K. J., et al. (2020). Magnetotail Dipolarization Fronts and Particle Acceleration: A Review. *Sci. China Earth Sci.* 63, 235–256. doi:10.1007/s11430-019-9551-y

Fu, H. S., Khotyaintsev, Y. V., André, M., and Vaivads, A. (2011). Fermi and Betatron Acceleration of Suprathermal Electrons behind Dipolarization Fronts. *Geophys. Res. Lett.* 38, a–n. doi:10.1029/2011GL048528

Gabrielse, C., Angelopoulos, V., Runov, A., and Turner, D. L. (2012). The Effects of Transient, Localized Electric Fields on Equatorial Electron Acceleration and Transport toward the Inner Magnetosphere. *J. Geophys. Res.* 117, a–n. doi:10.1029/2012JA017873

Gabrielse, C., Harris, C., Angelopoulos, V., Artemyev, A., and Runov, A. (2016). The Role of Localized Inductive Electric Fields in Electron Injections Around Dipolarizing Flux Bundles. *J. Geophys. Res. Space Phys.* 121, 9560–9585. doi:10.1002/2016JA023061

Gary, S. P., Hughes, R. S., Wang, J., and Chang, O. (2014). Whistler Anisotropy Instability: Spectral Transfer in a Three-dimensional Particle-in-cell Simulation. *J. Geophys. Res. Space Phys.* 119, 1429–1434. doi:10.1002/2013JA019618

Gary, S. P. (2015). Short-wavelength Plasma Turbulence and Temperature Anisotropy Instabilities: Recent Computational Progress. *Phil. Trans. R. Soc. A* 373, 20140149. doi:10.1098/rsta.2014.0149

Gary, S. P. (1993). "Theory of Space Plasma Microinstabilities," in *Cambridge Atmospheric and Space Science Series* (Cambridge: Cambridge University Press). doi:10.1017/CBO9780511551512

Hones, E. W., Jr. (1979). Transient Phenomena in the Magnetotail and Their Relation to Substorms. *Space Sci. Rev.* 23, 393–410. doi:10.1007/bf00172247

Hyman, J. M. (1983). Accurate Monotonicity Preserving Cubic Interpolation. *SIAM J. Sci. Stat. Comput.* 4, 645–654. doi:10.1137/0904045

Khotyaintsev, Y. V., Cully, C. M., Vaivads, A., André, M., and Owen, C. J. (2011). Plasma Jet Braking: Energy Dissipation and Nonadiabatic Electrons. *Phys. Rev. Lett.* 106, 165001. doi:10.1103/PhysRevLett.106.165001

Le Contel, O., Nakamura, R., Breuillard, H., Argall, M. R., Graham, D. B., Fischer, D., et al. (2017). Lower Hybrid Drift Waves and Electromagnetic Electron Space-phase Holes Associated with Dipolarization Fronts and Field-Aligned Currents Observed by the Magnetospheric Multiscale Mission during a Substorm. *J. Geophys. Res. Space Phys.* 122, 236. doi:10.1002/2017JA024550

Le Contel, O., Roux, A., Jacquey, C., Robert, P., Berthomier, M., Chust, T., et al. (2009). Quasi-parallel Whistler Mode Waves Observed by THEMIS during Near-Earth Dipolarizations. *Ann. Geophys.* 27, 2259–2275. doi:10.5194/angeo-27-2259-2009

Lezniak, T. W., Arnoldy, R. L., Parks, G. K., and Winckler, J. R. (1968). Measurement and Intensity of Energetic Electrons at the Equator at 6.6Re. *Radio Sci.* 3, 710–714. doi:10.1002/rds196837710

Li, H., Zhou, M., Deng, X., Yuan, Z., Guo, L., Yu, X., et al. (2015). A Statistical Study on the Whistler Waves behind Dipolarization Fronts. *J. Geophys. Res. Space Phys.* 120, 1086–1095. doi:10.1002/2014JA020474

Li, X., Baker, D. N., Temerin, M., Reeves, G. D., and Belian, R. D. (1998). Simulation of Dispersionless Injections and Drift Echoes of Energetic Electrons Associated with Substorms. *Geophys. Res. Lett.* 25, 3763–3766. doi:10.1029/1998gl900001

Liu, C. M., Fu, H. S., Liu, Y. Y., Wang, Z., Chen, G., Xu, Y., et al. (2020). Electron Pitch-Angle Distribution in Earth's Magnetotail: Pancake, Cigar, Isotropy, Butterfly, and Rolling-Pin. *J. Geophys. Res. Space Phys.* 125, e2020JA027777. doi:10.1029/2020JA027777

Liu, C. M., Fu, H. S., Xu, Y., Cao, J. B., and Liu, W. L. (2017). Explaining the Rolling-Pin Distribution of Suprathermal Electrons behind Dipolarization Fronts. *Geophys. Res. Lett.* 44, 6492–6499. doi:10.1002/2017GL074029

Liu, J., Angelopoulos, V., Runov, A., and Zhou, X.-Z. (2013). On the Current Sheets Surrounding Dipolarizing Flux Bundles in the Magnetotail: The Case for Wedgelets. *J. Geophys. Res. Space Phys.* 118, 2000–2020. doi:10.1002/jgra.50092

Moore, T. E., and Arnoldy, R. L. (1982). Plasma Pitch Angle Distributions Near the Substorm Injection Front. *J. Geophys. Res.* 87, 265–270. doi:10.1029/JA087iA01p00265

Nakamura, R., Baumjohann, W., Klecker, B., Bogdanova, Y., Balogh, A., Réme, H., et al. (2002). Motion of the Dipolarization Front during a Flow Burst Event Observed by Cluster. *Geophys. Res. Lett.* 29, 1942. doi:10.1029/2002gl015763

Nakamura, R., Baumjohann, W., Mouikis, C., Kistler, L. M., Runov, A., Volwerk, M., et al. (2004). Spatial Scale of High-Speed Flows in the Plasma Sheet Observed by Cluster. *Geophys. Res. Lett.* 31, a–n. doi:10.1029/2004GL019558

Nakamura, R., Baumjohann, W., Panv, E., Volwerk, M., Birn, J., Artemyev, A., et al. (2012). Flow Bouncing and Electron Injection Observed by Cluster. *J. Geophys. Res.* 118, 2055. doi:10.1002/jgra.50134

Northrop, T. G. (1963). *The Adiabatic Motion of Charged Particles*. New York: Interscience.

Pan, Q., Ashour-Abdalla, M., Walker, R. J., and El-Alaoui, M. (2014). Electron Energization and Transport in the Magnetotail during Substorms. *J. Geophys. Res. Space Phys.* 119, 1060–1079. doi:10.1002/2013JA019508

Panov, E. V., Kubyshkina, M. V., Nakamura, R., Baumjohann, W., Angelopoulos, V., Sergeev, V. A., et al. (2013). Oscillatory Flow Braking in the Magnetotail: THEMIS Statistics. *Geophys. Res. Lett.* 40, 2505–2510. doi:10.1002/grl.50407

Panov, E. V., Nakamura, R., Baumjohann, W., Angelopoulos, V., Petrukovich, A. A., Retinò, A., et al. (2010a). Multiple Overshoot and Rebound of a Bursty Bulk Flow. *Geophys. Res. Lett.* 37, L8103. doi:10.1029/2009GL041971

Panov, E. V., Nakamura, R., Baumjohann, W., Sergeev, V. A., Petrukovich, A. A., Angelopoulos, V., et al. (2010b). Plasma Sheet Thickness during a Bursty Bulk Flow Reversal. *J. Geophys. Res.* 115, a–n. doi:10.1029/2009JA014743

Parks, G. K., and Winckler, J. R. (1968). Acceleration of Energetic Electrons Observed at the Synchronous Altitude during Magnetospheric Substorms. *J. Geophys. Res.* 73, 5786–5791. doi:10.1029/ja073i017p05786

Pontius, D. H., and Wolf, R. A. (1990). Transient Flux Tubes in the Terrestrial Magnetosphere. *Geophys. Res. Lett.* 17, 49–52. doi:10.1029/gl017i001p00049

Runov, A., Angelopoulos, V., Gabrielse, C., Zhou, X.-Z., Turner, D., and Plaschke, F. (2013). Electron Fluxes and Pitch-Angle Distributions at Dipolarization Fronts: THEMIS Multipoint Observations. *J. Geophys. Res. Space Phys.* 118, 744–755. doi:10.1002/jgra.50121

Runov, A., Angelopoulos, V., Sitnov, M. I., Sergeev, V. A., Bonnell, J., McFadden, J. P., et al. (2009). THEMIS Observations of an Earthward-Propagating Dipolarization Front. *Geophys. Res. Lett.* 36, L14106. doi:10.1029/2009GL038980

Runov, A., Angelopoulos, V., and Zhou, X.-Z. (2012). Multipoint Observations of Dipolarization Front Formation by Magnetotail Reconnection. *J. Geophys. Res.* 117, a–n. doi:10.1029/2011JA017361

Runov, A., Angelopoulos, V., Zhou, X.-Z., Zhang, X.-J., Li, S., Plaschke, F., et al. (2011). A THEMIS Multicase Study of Dipolarization Fronts in the Magnetotail Plasma Sheet. *J. Geophys. Res.* 116, A05216. doi:10.1029/2010JA016316

Sergeev, V. A., Angelopoulos, V., Apatenkov, S., Gosling, J. T., Cattell, C. A., and Russell, C. T. (1996). Detection of Localized, Plasma-Depleted Flux Tubes or Bubbles in the Midtail Plasma Sheet. *J. Geophys. Res.* 101, 10,817–10,826. doi:10.1029/96ja00460

Sergeev, V., Angelopoulos, V., Apatenkov, S., Bonnell, J., Ergun, R., Nakamura, R., et al. (2009). Kinetic Structure of the Sharp Injection/dipolarization Front in the Flow-Braking Region. *Geophys. Res. Lett.* 36, L21105. doi:10.1029/2009GL040658

Smets, R., Delcourt, D., Sauvaud, J. A., and Koperski, P. (1999). Electron Pitch Angle Distributions Following the Dipolarization Phase of a Substorm: Interball-Tail Observations and Modeling. *J. Geophys. Res.* 104, 14571–14581. doi:10.1029/1998JA900162

Tsyganenko, N. A. (1987). Global Quantitative Models of the Geomagnetic Field in the Cislunar Magnetosphere for Different Disturbance Levels. *Planet. Space Sci.* 35, 1347–1358. doi:10.1016/0032-0633(87)90046-8

Vasyliunas, V. M. (1968). A Survey of Low-Energy Electrons in the Evening Sector of the Magnetosphere with OGO 1 and OGO 3. *J. Geophys. Res.* 73, 2839–2884. doi:10.1029/ja073i009p02839

Viberg, H., Khotyaintsev, Y. V., Vaivads, A., André, M., Fu, H. S., and Cornilleau-Wehrlin, N. (2014). Whistler Mode Waves at Magnetotail Dipolarization Fronts. *J. Geophys. Res. Space Phys.* 119, 2605–2611. doi:10.1002/2014JA019892

Wolf, R. A., Wan, Y., Xing, X., Zhang, J.-C., and Sazykin, S. (2009). Entropy and Plasma Sheet Transport. *J. Geophys. Res.* 114, a–n. doi:10.1029/2009JA014044

Wu, M., Lu, Q., Volwerk, M., Vörös, Z., Zhang, T., Shan, L., et al. (2013). A Statistical Study of Electron Acceleration behind the Dipolarization Fronts in the Magnetotail. *J. Geophys. Res. Space Phys.* 118, 4804–4810. doi:10.1002/jgra.50456

Wu, P., Fritz, T. A., Larvaud, B., and Lucek, E. (2006). Substorm Associated Magnetotail Energetic Electrons Pitch Angle Evolutions and Flow Reversals: Cluster Observation. *Geophys. Res. Lett.* 33. doi:10.1029/2006GL026595

Zaharia, S., Cheng, C. Z., and Johnson, J. R. (2000). Particle Transport and Energization Associated with Substorms. *J. Geophys. Res.* 105, 18,741. doi:10.1029/1999ja000407

Zelenyi, L. M., Lominadze, J. G., and Taktakishvili, A. L. (1990). Generation of the Energetic Proton and Electron Bursts in Planetary Magnetotails. *J. Geophys. Res.* 95, 3883–3891. doi:10.1029/JA095iA04p03883

Zhang, X., Angelopoulos, V., Artemyev, A. V., and Liu, J. (2018). Whistler and Electron Firehose Instability Control of Electron Distributions in and Around Dipolarizing Flux Bundles. *Geophys. Res. Lett.* 45, 9380–9389. doi:10.1029/2018GL079613

Zhao, M. J., Fu, H. S., Liu, C. M., Chen, Z. Z., Xu, Y., Giles, B. L., et al. (2019). Energy Range of Electron Rolling Pin Distribution behind Dipolarization Front. *Geophys. Res. Lett.* 46, 2390–2398. doi:10.1029/2019GL082100

Zhou, M., Ashour-Abdalla, M., Deng, X., Schriver, D., El-Alaoui, M., and Pang, Y. (2009). THEMIS Observation of Multiple Dipolarization Fronts and Associated Wave Characteristics in the Near-Earth Magnetotail. *Geophys. Res. Lett.* 36, 20107. doi:10.1029/2009GL040663

Conflict of Interest: The authors declare that the research was conducted in the absence of any commercial or financial relationships that could be construed as a potential conflict of interest.